Melanin Pigmentation in Rat Eyes: In Vivo Imaging by Polarization-Sensitive Optical Coherence Tomography and Comparison to Histology

Bernhard Baumann,[1] Johannes Schirmer,[1] Sabine Rauscher,[2] Stanislava Fialová,[1] Martin Glösmann,[3] Marco Augustin,[1] Michael Pircher,[1] Marion Gröger,[2] and Christoph K. Hitzenberger[1]

[1]Center for Medical Physics and Biomedical Engineering, Medical University of Vienna, Vienna, Austria
[2]Core Facility Imaging, Medical University of Vienna, Vienna, Austria
[3]Core Facility for Research and Technology, University of Veterinary Medicine Vienna, Vienna, Austria

Correspondence: Bernhard Baumann, Center for Medical Physics and Biomedical Engineering, Medical University of Vienna, Währinger Gürtel 18-20, 4L, 1090 Vienna, Austria; bernhard.baumann@meduniwien.ac.at.

Submitted: July 20, 2015
Accepted: October 8, 2015

Citation: Baumann B, Schirmer J, Rauscher S, et al. Melanin pigmentation in rat eyes: in vivo imaging by polarization-sensitive optical coherence tomography and comparison to histology. *Invest Ophthalmol Vis Sci*. 2015;56:7462–7472. DOI:10.1167/iovs.15-17742

Purpose. The purpose of this study was to demonstrate polarization-sensitive optical coherence tomography (PS-OCT) for imaging pigmented structures in the posterior eye segments of albino and pigmented rats and to correlate depolarization contrast of the retinal pigment epithelium (RPE) and choroid in in vivo PS-OCT to melanin pigmentation detected in postmortem histologic serial sections.

Methods. In vivo three-dimensional PS-OCT imaging was performed in adult albino and pigmented rat eyes at 70-kHz A-line rate. Degree of polarization uniformity (DOPU) fundus maps and radial DOPU profiles were generated. Postmortem histomorphologic analysis was performed in order to investigate melanin pigmentation of the RPE and choroid. Fundus pigmentation maps were extracted from histologic serial sections. Pigmentation profiles were correlated to DOPU profiles of the same eyes.

Results. Strong depolarization was found in the RPE/choroid complex of pigmented rats, whereas the same structures exhibited uniform polarization in albino rats. The difference between the depolarization characteristics between albino and pigmented animals was statistically significant. In the fundus pigmentation maps, optical pigment density was zero in albino rat eyes. In pigmented rat eyes, a strong negative correlation between optical pigment density and DOPU was observed.

Conclusions. This in vivo and ex vivo investigation of posterior rat eyes indicates that melanin is the cause of depolarization in retinal PS-OCT images. It further demonstrates that melanin pigmentation in the RPE and choroid can be quantified via depolarization imaging and therefore suggests that PS-OCT is a useful tool for the noninvasive quantitative assessment of pigmentary changes in vision-threatening diseases such as age-related macular degeneration.

Keywords: optical coherence tomography, polarization sensitive devices, melanin, depolarization, retinal pigment epithelium, choroid

The eye contains four different basic pigments: lutein, zeaxanthin, melanin, and lipofuscin. Lutein and zeaxanthin are accumulated in the retina. Zeaxanthin is most concentrated in the macula lutea and also provides the yellow color (lat. lutea = yellow), whereas lutein predominates the peripheral retina. Melanin is contained by the iris pigment epithelium, the ciliary body, the retinal pigment epithelium (RPE), and the choroid. Lipofuscin accumulates in the RPE. There, melanolipofuscin containing both melanin and lipofuscin can also be found.

Pigments play a vital role in vision. The macular pigment, that is, lutein and zeaxanthin, may have important biologic functions such as antioxidation and anti-inflammation. Further, lutein and zeaxanthin absorb blue light entering the eye and may therefore protect against retinal damage.[1] Melanin, too, acts as photo-screen against visible light and ultraviolet radiation and as an antioxidant.[2] The RPE lipofuscin accumulates with age and has been associated with the development of AMD.[3,4] Recent years have witnessed an increasing interest in the development of methods for assessing ocular pigmentation.

Optical imaging of biologic tissues provides high imaging resolution, high acquisition speed, and little to no contact/invasiveness. Therefore, optical methods for in vivo and in situ imaging of ocular pigmentation are of high interest for both preclinical, pathobiologic research of ocular diseases and clinical assessment in diagnostics and treatment response. In order to assess pigmented structures in the posterior eye, spectroscopic fundus photography, photoacoustic imaging, darkfield, and fluorescence-based methods have been developed.[5–10] Polarization of light depends on tissue microstructure and provides an alternative method for imaging tissue pigmentation. The potential of polarization-sensitive (PS) imaging methods such as scanning laser polarimetry and PS-optical coherence tomography (PS-OCT) for the assessment of pigmented ocular structures was recently demonstrated.[11–14] In contrast to other ocular tissues, light scattered by tissues

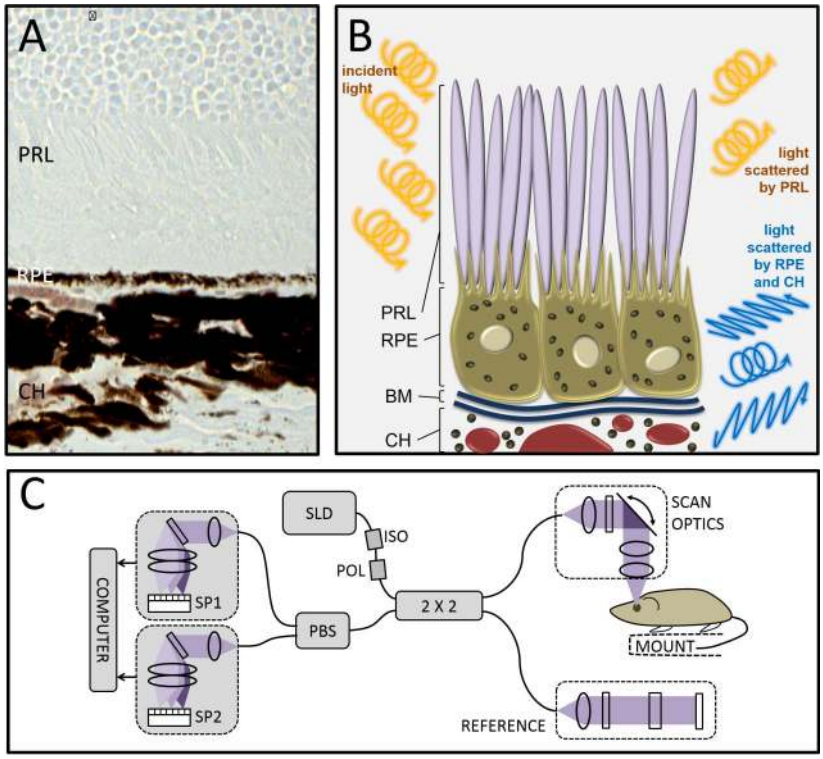

Figure 1. Polarization-sensitive–OCT and depolarization of light in the RPE and choroid. (**A**) Histologic cryosection of a pigmented rat eye. Beneath the photoreceptor layer (PRL), melanin pigments can be observed in the RPE and around the vasculature in the choroid (CH). (**B**) Cartoon illustrating polarization preserving and depolarizing characteristics of ocular tissues. Circularly polarized light (*left*) shone on the tissue retains its polarization state on backscattering by the PRL. In contrast, the polarization states of light backscattered by the pigmented RPE and CH are scrambled, that is, light loses its original polarization state and is depolarized. (**C**) Scheme of PS-OCT prototype for depolarization imaging in the rat eye. Light from an SLD illuminates a fiber interferometer (2 × 2) via an isolator (ISO) and a polarizer (POL). The PS-OCT signal is detected by a polarization sensitive detection unit featuring a polarizing beam splitter (PBS) and two identical spectrometer units (SP).

containing melanin is depolarized (Fig. 1). Polarization-sensitive imaging methods can measure depolarization of light and use it as a contrast channel. Polarization-sensitive–OCT has proven particularly useful for the segmentation of the retinal pigment epithelium,[12] a structure playing an essential role in AMD. Using depolarization—namely the degree of polarization uniformity (DOPU)—as a backbone for segmentation, PS-OCT enabled qualitative and quantitative imaging of retinal lesions such as drusen, zones of geographic atrophy, and RPE integrity in exudative AMD.[13,15–19] An advantage of polarization-based segmentation algorithms over those only relying on the reflectivity of ocular structures is their robustness to factors such as anterior eye tissue transparency and integrity, light absorption in retinal blood vessels, vignetting, and focus degradation due to aberrations. Thus far, depolarization was mainly used as a binary measure. That is, image pixels were rated either depolarizing or not depolarizing if the depolarization metric DOPU undercut or exceeded a threshold value. However, RPE depolarization varies between different subjects and is significantly reduced (or even absent) in subjects with albinism.[20–22] We therefore performed depolarization measurements in phantoms containing varying concentrations of melanin granules and found a negative exponential relation between melanin concentration and DOPU.[21] In this article, we aim to provide evidence that the results from measurements of synthetic melanin phantoms translate to real in vivo PS-OCT imaging results. Retinal PS-OCT imaging was performed in rats of three strains with different pigmentation. The depolarization characteristics of the RPE and choroid containing melanin pigments were analyzed in the peripapillary region. Pigmentation in postmortem eyes was then assessed in histologic sections and correlated to the depolarization characteristics in the corresponding in vivo images.

Methods

Animals

Pigmented and albino animals were investigated. Male Long-Evans rats ($N = 6$) and Brown Norway rats ($N = 8$) were purchased from Charles River Germany GmbH (Sulzfeld, Germany). Male Sprague-Dawley rats ($N = 3$) were obtained from the breeding facility at the Medical University of Vienna (Vienna, Austria). The rats were kept under controlled lighting conditions (12-hour light, 12-hour dark). For the imaging experiments, rats were anaesthetized using ketamine (Ketasol; aniMedica GmbH, Senden, Germany; 80 mg/kg body weight; intraperitoneal) and xylazine (Rompun; Bayer Austria GmbH, Vienna, Austria; 8 mg/kg body weight; intraperitoneal). Anesthesia was required in order to immobilize the animal for PS-OCT imaging. The pupils were dilated using phenylephrine (2.5%; topical) and tropicamide (Mydriaticum; Agepha Pharmaceuticals, Vienna, Austria; topical). All experiments were performed in accordance with the ARVO Statement for the Use of Animals in Ophthalmic and Vision Research and under a protocol approved by the ethics committee at Medical University of Vienna and the Austrian Federal Ministry of Science, Research and Economy (protocol no. GZ 66.009/0072-WF/V/3b/2015).

Polarization-Sensitive–OCT

The PS-OCT imaging was performed with a prototype instrument presented earlier.[23] The system is based on spectral domain PS-OCT technology using polarization maintaining fiber optics (Fig. 1C). A superluminescent diode (SLD; Superlum, Ireland) centered at 837 nm and covering a bandwidth of 52 nm was used as a light source. The measured axial resolution was 7.6 μm in air, corresponding to 5.6 μm in tissue ($n = 1.35$). The light illuminating the eye was circularly polarized. Light backscattered by ocular structures was interfered with the reference beam and detected using a pair of identical spectrometers based on high-speed line scan cameras (Basler AG, Ahrensburg, Germany). The PS-OCT system was operated at a line rate of 70 kHz.

For retinal imaging, animals were anesthetized as described above. The rats were placed in a custom-made mount that enabled the alignment of the animal eye with respect to the measurement beam. Beam diameter and power at the cornea were 0.85 mm and 700 μW, respectively. The retina was raster scanned using galvanometer scanners. With a scan field of 23° × 23°, PS-OCT data cubes covering a region of 1.5 (x) × 1.5 (y) × 2.7 mm (z; optical distance with $n = 1.35$) were recorded around the optic nerve head (ONH). Based on a rat eye model reported in the literature, scan angles were converted to distances on the retina using a constant factor of 65 μm/degree scan angle.[24] Each data set comprised 512 (x) × 400 (y) × 1024 (z) voxels and was acquired in approximately 3 seconds.

Depolarization Analysis

Depolarization in PS-OCT data sets was analyzed in the RPE and choroid region. First, standard OCT processing was performed for each of the two polarization channels. From the OCT signals of the two channels, the Stokes vector elements [Q, U, V] describing the polarization state in each image pixel were computed. The Stokes vector elements were averaged in rectangular kernels sized 6 (x) × 7 (z) pixels. This kernel size was found empirically and provided a good compromise of reliable polarization statistics and decent spatial resolution. Thereby, only pixels exceeding an intensity 8 dB above the average noise level were included in the calculations. Also, averaging was performed within the evaluation window only when more than 20% of the pixels within (i.e., eight pixels for a kernel size of 6 × 7) met the intensity threshold. Pixels that did not meet this criterion were displayed in gray. From the averaged Stokes vector elements, DOPU was calculated as the root of the summed squared Stokes vector elements normalized by the pixel intensity.[12] DOPU images were displayed as two- and three-dimensional color images, with blue indicating low DOPU, that is, strong depolarization as in pigmented tissues, and red indicating high DOPU close to unity, that is, uniform polarization within the evaluation window as in the neural retina.

The depolarization properties in the RPE and choroid were analyzed by segmenting the RPE/choroid complex and generating DOPU fundus maps. For this purpose, the reflectivity images were first smoothed by an 8 × 8-pixel median filter, and the steep intensity step at the vitreoretinal interface was segmented. By advancing this first segmentation line 80 pixels (~110 μm) in the posterior direction, the RPE was found similar to a previously described method,[25] and an evaluation band with a user-defined length was fit around the RPE/choroid complex. Both mean and minimum DOPUs were computed within this evaluation band for each A-scan and mapped as $DOPU_{mean}$ and $DOPU_{min}$ fundus maps. Upon identification of the center of the ONH on reflectivity fundus projection maps, radial $DOPU_{min}$ and $DOPU_{mean}$ profiles were computed by annular averaging the respective maps. The central disk (showing the ONH) with radius $r < 180$ μm was excluded from the profile computation.

Histology

For histomorphologic analysis, animals were euthanized with an overdose of sodium pentobarbital (Release ad usum veterinarium). The eyes were enucleated within minutes after death, carefully slit open at the limbus, and fixed in paraformaldehyde (PFA; 4%). After 24 hours, cornea and lens were removed. The eye cup was then fixed in PFA for another 24 to 48 hours. The eyes were cryoprotected in increasing sucrose concentrations. After embedding in optimal cutting temperature compound (Tissue-Tek, Sakura Finetek Europe B.V., Alphen aan den Rijn, The Netherlands) mixed with 20% sucrose, the eyes were frozen for cryosectioning at −20°C. Using a cryotome (Leica Biosystems Nussloch GmbH, Nussloch, Germany), the frozen tissue blocks were cut into 5-μm-thick transverse sections. For serial sectioning, histologic sections were made every 25 μm over 1 mm centered at the ONH, resulting in 80 sections per eye. The sections were digitized with a TissueFAXS slide scanner (TissueGnostics, Vienna, Austria). Selected histologic sections were also imaged with a bright field microscope (Axio Imager, Zeiss, Carl Zeiss AG, Oberkochen, Germany).

Pigmentation Analysis of Histologic Sections

Melanin pigmentation was analyzed in the serial sections of pigmented rat eyes. Using homemade software, the image stacks were loaded and aligned such that rotation and translation between subsequent images was removed. In order to assess melanin pigmentation in the unstained slides, the respective image pixels were robustly segmented by decomposing the color image into its RGB channels. The light brown to dark brown hue of melanin granules in the RPE, choroid, and some of the vasculature was decoded as pixels that met all of the following conditions: (1) R ≥ G, (2) R ≥ B, and (3) R + G + B < 340, where R, G, and B denote the intensity of the red, green, and blue color channels with a resolution of 8 bits each. Pixels identified by the above conditions were weighed with the original pixel intensity, that is, the sum of R, G, and B. The resulting aligned images were then saved as 16-bit grayscale images. From these pigmentation images, fundus pigmentation maps were generated by computing the axially integrated pigmentation value, henceforth termed optical pigment density (OPD), for each transverse location. Analogous to the $DOPU_{mean}$(r) profiles produced from the in vivo PS-OCT data, radial OPD(r) profiles were computed by manual identification of the center of the ONH and annular averaging of OPD.

Statistical Analysis

Statistical comparison between average DOPU in the left and right eyes of pigmented and albino animals was performed by means of a paired-samples two-tailed Student's t-test. $P < 0.05$ was considered statistically significant. The correlation of DOPU values and OPD values at the same eccentricity was investigated by computing Spearman's rank correlation. Spearman's ρ values $\rho < -0.5$ and $\rho > 0.5$ were interpreted as strong negative and positive correlation, respectively. Linear regression analysis was performed to find the relation between DOPU and OPD.

Results

In Vivo Depolarization Imaging

Pigmented Brown Norway and Long-Evans rats, as well as albino Sprague-Dawley rats, were imaged with PS-OCT. Figure 2 shows volume renderings of reflectivity data (as in regular

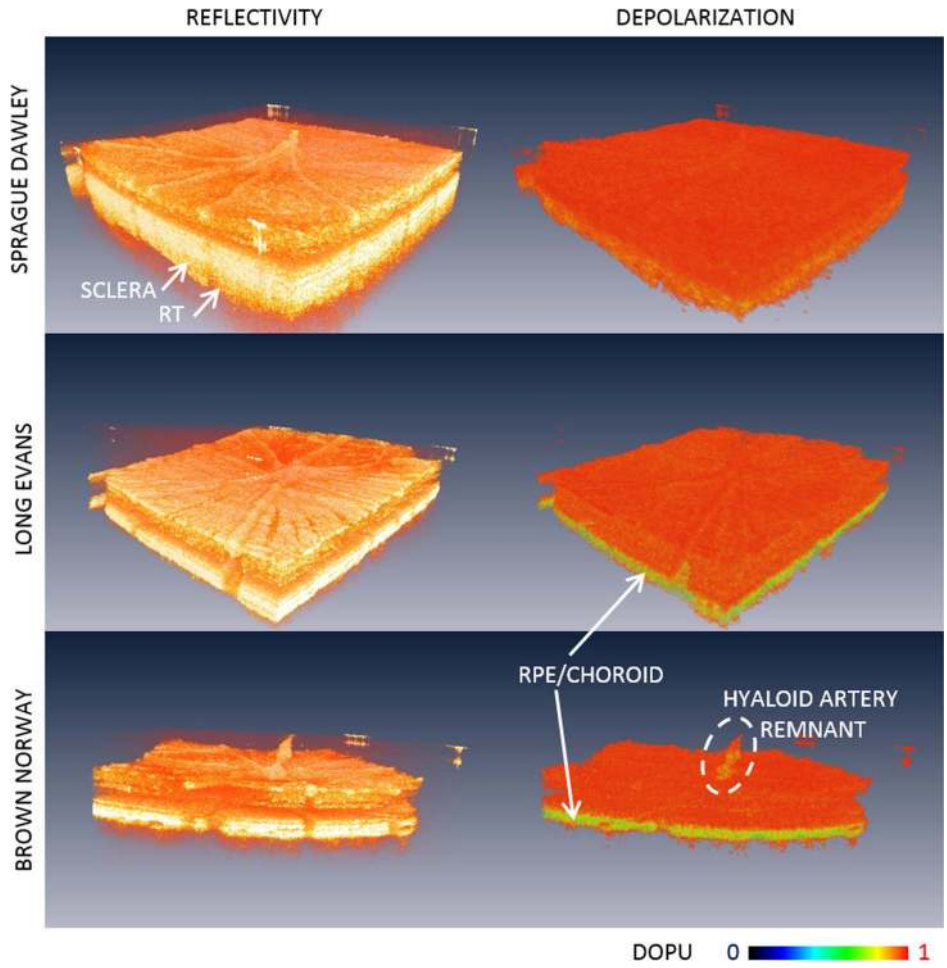

Figure 2. Three-dimensional imaging of depolarization in the posterior eye segment of pigmented and albino rats. (**Left**) Volume renderings of reflectivity data around the ONH. The layered structure of the retina can be observed. In the albino Sprague-Dawley rat, posterior structures such as choroid, sclera, and even some retrobulbar tissue (RT) can be observed. In contrast, light penetration is limited by the densely pigmented, hyperscattering choroid in the pigmented Long-Evans and Brown Norway rats. (**Right**) The DOPU images depict the corresponding depolarization characteristics. While the albino rat eye exhibits generally uniform polarization, lower DOPU values due to depolarization can be observed in the pigmented RPE and choroid of the Long-Evans and Brown Norway rats. In the latter eye, also the remnant of the hyaloid artery is depolarizing and appears *yellow/greenish* in the DOPU image.

OCT imagery) and DOPU data. In the reflectivity images, structural features such as the major retinal vessels, retinal nerve fiber bundles, and the retinal layers can be observed in all rats. When comparing the albino rats to the pigmented animals, deep penetration beyond the choroid into the sclera and even into the retrobulbar space was visible. In contrast, the pigmented animals exhibited higher backscatter signals from the pigmented RPE/choroid complex. The DOPU images in the right column revealed the depolarization properties of the same PS-OCT data sets. In Sprague-Dawley rats, uniformly high DOPU values were observed in the retina and choroid. Only a slight decrease was apparent as orange hue in the highly birefringent sclera, since polarization states slightly changed within the evaluation kernel. The retinal DOPU characteristics were quite similar in the pigmented Long-Evans and Brown Norway rat retinas. However, the melanin-laden RPE/choroid complexes stood out with lower DOPU values in the green color. Further, in the Brown Norway rat, depolarization was also observed in the pigmented remnant of the hyaloid artery.

Reflectivity and DOPU B-scan images are shown in Figure 3. Again, most structures exhibited high DOPU values indicating uniform polarization states, whereas lower DOPU values indicate depolarization was only observed in the pigmented RPE and choroid of the Brown Norway and Long-Evans rats. Also here, the innermost part of the ONH structure, that is, the remnant of the hyaloid canal, which we did not observe in all animals, was depolarizing and appeared greenish. In Figures 3E and F, the region used for analyzing depolarization in the RPE/choroid complex is indicated by dashed blue lines.

Depolarization fundus maps were generated from both left and right eyes of six Brown Norway rats, five Long-Evans rats, and three Sprague-Dawley rats. Exemplary fundus maps of left and right eyes are shown in Figure 4A. The reflectivity fundus projection maps provide an overview of the scanned locations. Adjacent to the right, $DOPU_{min}$ maps are shown. While in the albino rat (top row) the $DOPU_{min}$ maps are mostly orange, their counterparts derived from the pigmented eyes are green and blue at lower DOPU values. Yet, the overall appearance of the DOPU maps is consistent when comparing left and right eyes in the same animal. Radial $DOPU_{min}$ profiles are shown in Figure 4B. Radial traces of albino animals are displayed in red color, whereas pigmented animals are plotted in gray and blue. Different shades correspond to different animals. In general, uniformly high $DOPU_{min}$ profiles were observed in the albino rats. $DOPU_{min}$ was 0.86 ± 0.01 (mean ± SD) and 0.84 ± 0.01

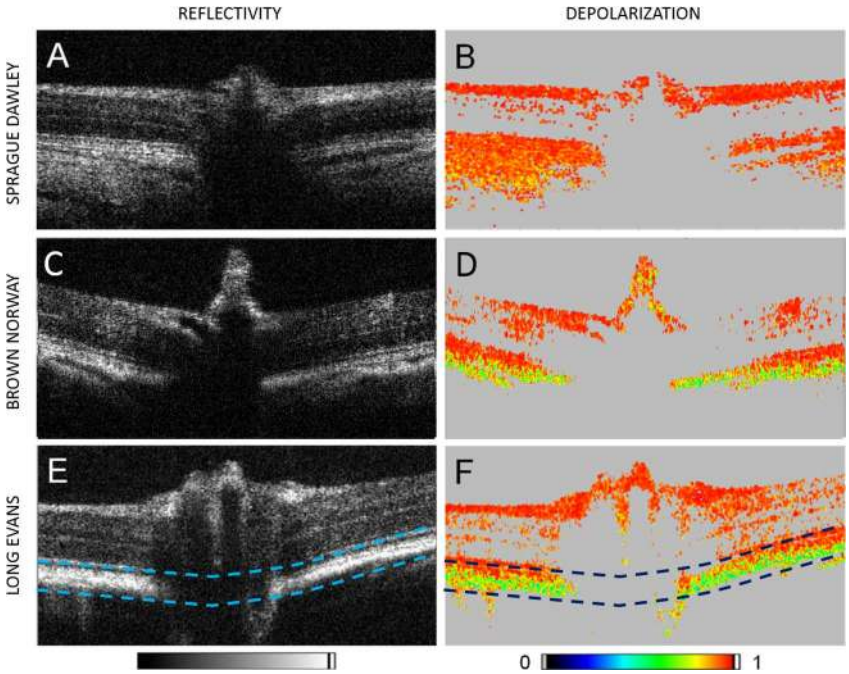

FIGURE 3. Reflectivity and DOPU B-scan images of the albino Sprague-Dawley rat, the pigmented Brown Norway rat, and the pigmented Long-Evans rat also shown in Figure 2. In the DOPU images, polarization preserving structures exhibit high DOPU values and appear *reddish*, whereas lower DOPU values can be observed in depolarizing structures (*greenish color*). The dashed blue lines in the bottom row indicate the range used for the depolarization analysis.

in the left and right eyes of albino rats, and 0.42 ± 0.06 (Brown Norway: 0.46 ± 0.06; Long-Evans: 0.38 ± 0.03) and 0.41 ± 0.06 (Brown Norway: 0.45 ± 0.06; Long-Evans: 0.37 ± 0.04) in the left and right eyes of pigmented rats, respectively. Neither in albino nor in pigmented animals were any statistically significant differences of the average $DOPU_{min}$ values found between left and right eyes ($P = 0.084$ and $P = 0.339$, respectively). However, the difference between the depolarization characteristics (average $DOPU_{min}$) in albino and pigmented rats was statistically highly significant ($P < 0.0001$; Fig. 4D). Furthermore, a statistically significant difference between $DOPU_{min}$ values was found between the two pigmented rat strains ($P = 0.013$ and $P = 0.011$ for the left and right eyes, respectively). In Figure 4C, radial $DOPU_{mean}$ profiles computed from the same data sets are shown. Similar to the $DOPU_{min}$ characteristics, $DOPU_{mean}$ is considerably higher in the left and right eyes of albino rats (0.90 ± 0.02 and 0.92 ± 0.01, respectively) than in those of pigmented rats (0.73 ± 0.06 and 0.73 ± 0.04, respectively). $DOPU_{mean}$ was 0.75 ± 0.07 and 0.75 ± 0.03 for the left and right eyes of Brown Norway rats and 0.71 ± 0.03 and 0.71 ± 0.05 for Long-Evans rats, respectively. Also, for the average $DOPU_{mean}$, the difference between depolarization characteristics in albino and pigmented rats was statistically highly significant ($P < 0.005$; Fig. 4E). In contrast to the statistically significant difference of $DOPU_{min}$ beween Brown Norway and Long-Evans rats, $DOPU_{mean}$ was not sensitive enough to detect a difference regarding depolarization between the two pigmented rat strains ($P = 0.152$ and $P = 0.099$ for the left and right eyes, respectively).

Ex Vivo Melanin Pigmentation Assessment

Histologic analysis following in vivo PS-OCT imaging was performed in two Brown Norway rats, one Long-Evans rat, and one Sprague-Dawley rat. Exemplary micrographs of histologic sections are shown in Figure 5. Melanin pigmentation was mapped and analyzed using OPD profiles only in the pigmented Brown Norway and Long-Evans rats, because the Sprague-Dawley rats only produced blank images due to the lack of pigmentation (and, therefore, of brown pixels in histologic sections). In other words, OPD was always zero in albino rats.

The $DOPU_{mean}$ profiles of the left and right eyes of the pigmented rats are shown in Figures 6A and B, respectively. Again, rather uniform depolarization profiles can be observed. Close to the ONH, DOPU values are slightly lower. A good correspondence between left and right eyes is demonstrated in Figure 6C, where DOPU values at the same eccentricity are plotted for left and right eyes. The gray dashed line indicates the line of perfect overlap of DOPU values in left and right eyes.

The OPD profiles generated from the histologic sections of the same animals postmortem are shown in Figures 6D and E for the left and right eyes, respectively. In general, higher OPD values can be observed in the vicinity of the ONH. However, differences in the OPD profiles are obvious between left and right eyes of the same animals. These are also pronounced in Figure 6F, where OPD of the left eyes is plotted against OPD for the corresponding right eyes at the same eccentricities. From the deviation of the OPD data from the gray dashed $X = Y$ line, differences between OPD in the left and right eyes can be observed.

In order to assess the relation between depolarization in PS-OCT images and melanin pigmentation in the corresponding histologic samples, OPD(r) was plotted as a function of DOPU(r) in Figure 6G. Here, the different gray and blue levels denote the six pigmented eyes. A negative trend from higher OPD at low DOPU toward lower OPD at higher DOPU can be observed. Spearman's rank correlation of the pooled data set

Investigative Ophthalmology & Visual Science

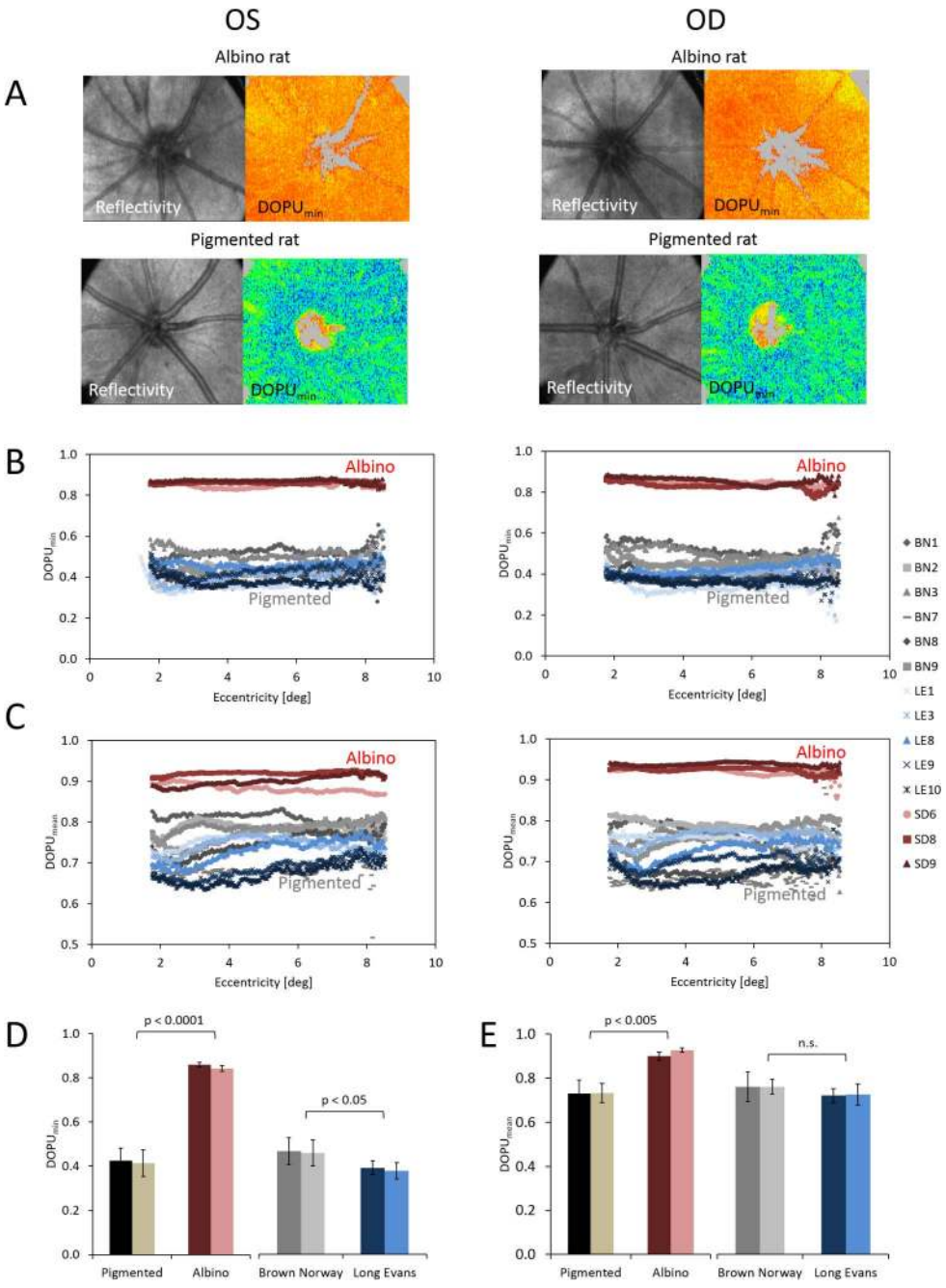

Figure 4. Analysis of depolarization characteristics: OS and OD denote the left and right eyes, respectively. (**A**) Exemplary fundus maps of reflectivity and $DOPU_{min}$. Peripapillary tissue in the RPE/choroid of albino rats is polarization preserving at high DOPU values (*top row*). In pigmented animals, these tissues exhibit depolarization at low DOPU values (*bottom row*). (**B**) Radial $DOPU_{min}$ profiles centered at the ONH demonstrate the uniform, polarization-preserving characteristics in albino eyes (data shown in *red*) versus the depolarizing behavior of pigmented animals (data shown in *gray* and *blue* for Brown Norway and Long-Evans rats, respectively). SD, Sprague-Dawley rats; BN, Brown Norway rats; LE, Long-Evans rats. (**C**) Radial $DOPU_{mean}$ profiles centered at the ONH computed from the same data sets. (**D**, **E**) Average $DOPU_{min}$ (**D**) and $DOPU_{mean}$ (**E**) in the left and right eyes of pigmented rats (*brown bars*) versus albino rats (*red bars*). Although there was no statistically significant difference between the left and right eyes within each group, DOPU was significantly different between the albino and pigmented groups. On the *right*, average $DOPU_{min}$ (**D**) and $DOPU_{mean}$ (**E**) in the left and right eyes of Brown Norway rats (*gray bars*) versus Long-Evans rats (*blue bars*) are shown. A statistically significant difference was only found by comparing $DOPU_{min}$ values.

showed a strong negative correlation of OPD and DOPU with Spearman's $\rho = -0.756$). A linear regression of the data gave $OPD = -69{,}245 \times DOPU + 60{,}894$, which is plotted as a gray dashed line in Figure 6G. Also, two data points representing the average DOPU values from the left and right eyes of an albino rat were plotted (red circles with $OPD = 0$).

Discussion

Melanin pigmentation is an important component for normal vision in humans. Ocular structures containing melanin granules, namely the uvea and the pigment epithelium, and their role in diseases such as AMD have been subject to

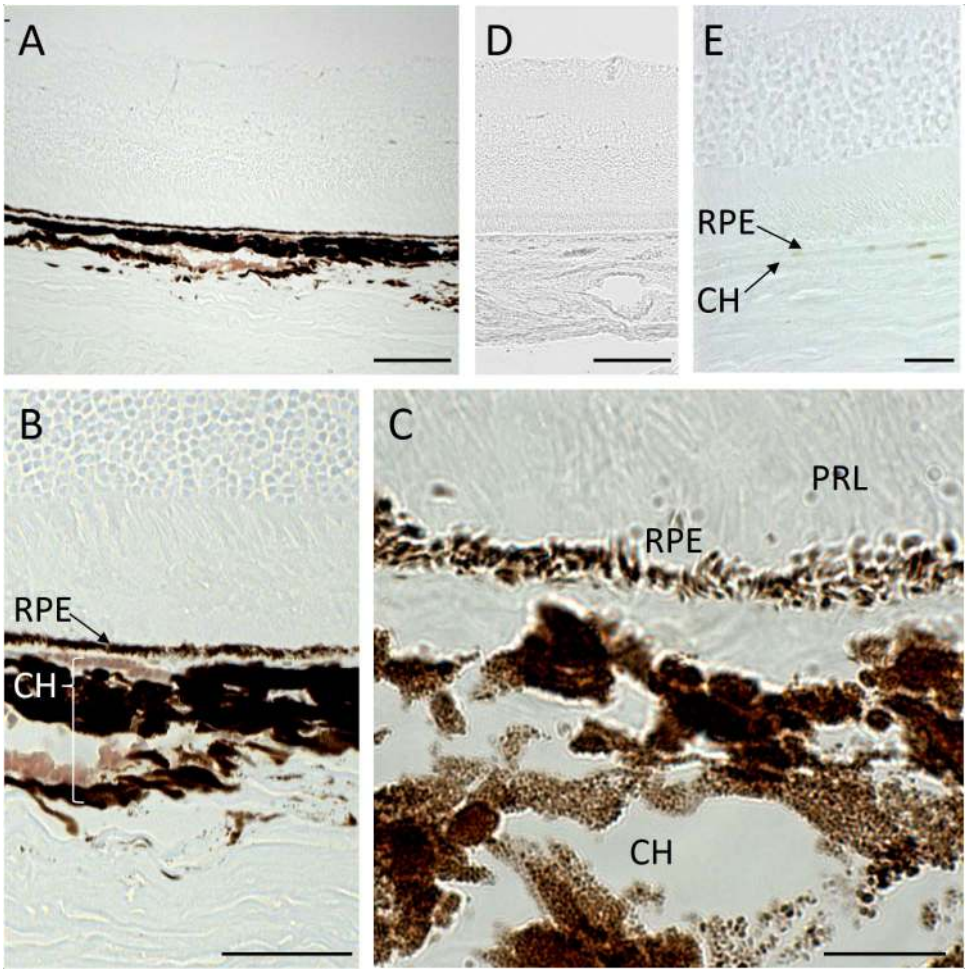

Figure 5. Bright field micrographs of unstained 5-μm-thick cryosections. (**A–C**) Different magnification views visualize the brown melanin granules in the RPE and choroid of Brown Norway rats. (**D**, **E**) No melanin granules can be observed in albino Sprague-Dawley rat retinas. *Scale bars*: 100 (**A**, **D**), 50 (**B**), 20 (**E**), and 10 μm (**C**).

investigations using methods ranging from fundus photography to electron microscopy.[10,26–31] In particular, the melanin-containing structures in the posterior eye—the RPE and the choroid—are of great interest for understanding the etiology of AMD and hence for the development of modalities for early diagnosis and treatment.

Fundus imaging methods developed for quantitative imaging of melanin in the RPE and choroid are based on a variety of different technologies. Multispectral color fundus photography fits reflectance of different colors to histologically determined pigment concentrations but may be obscured by absorbers and scatterers in the anterior eye, lens, and vitreous.[5] Autofluorescence-based methods have emerged in the last decade as a powerful tool for the assessment of lipofuscin in the RPE. Fundus autofluorescence (FAF) has proven particularly useful for mapping RPE atrophy in nonexudative AMD.[29] Recently, near infrared FAF was demonstrated for imaging melanin autofluorescence in the RPE and choroid[8] and was reported for imaging pigmentary abnormalities in diseases such as central serous chorioretinopathy, Stargardt, and AMD.[32–35] Similar to fundus photography, FAF signals from the retina are prone to influence from optical components in the imaging apparatus, as well as to overlap of signals from different retinal structures, some of which can be overcome by normalization methods in order to provide so-called quantitative FAF imaging.[36,37] Recently developed fluorescence lifetime imaging ophthalmoscopy (FLIO) was demonstrated in mice and may in the future enable the differentiation and quantification of pigments in the posterior eye segment.[38] Finally, photoacoustic imaging enables specific imaging of chromophores such as hemoglobin and melanin. Photoacoustic imaging of melanin pigmentation in the retina was successfully demonstrated in the eyes of pigmented and albino rats. However, at the moment, this technique requires expensive femtosecond lasers and high probe powers at the eye.[6] Melanin imaging using PS-OCT—as demonstrated here—can be performed rapidly, three dimensionally, and with high resolution. The PS-OCT approach presented here might represent a feasible alternative for quantitative assessment of melanin pigmentation in the posterior eye via depolarization. It should be noted that there are various definitions of depolarization. In DOPU imagery, depolarization refers to the scrambling of polarization states of neighboring speckles. Thereby, only coherently detected light contributes to the DOPU signal. Thus, the degree of polarization computed only for a single pixel would always be 1.[39]

In this study, three-dimensional imaging of the pigmented layers was performed in the rat eye. The layered structure of the rat retina is similar to that of the human retina, except rats do not have a fovea. Melanin granules are located in the RPE and choroid.[40] $DOPU_{min}$ measurements around the rat ONH yielded values of 0.42 ± 0.06 and 0.41 ± 0.06 for the left and

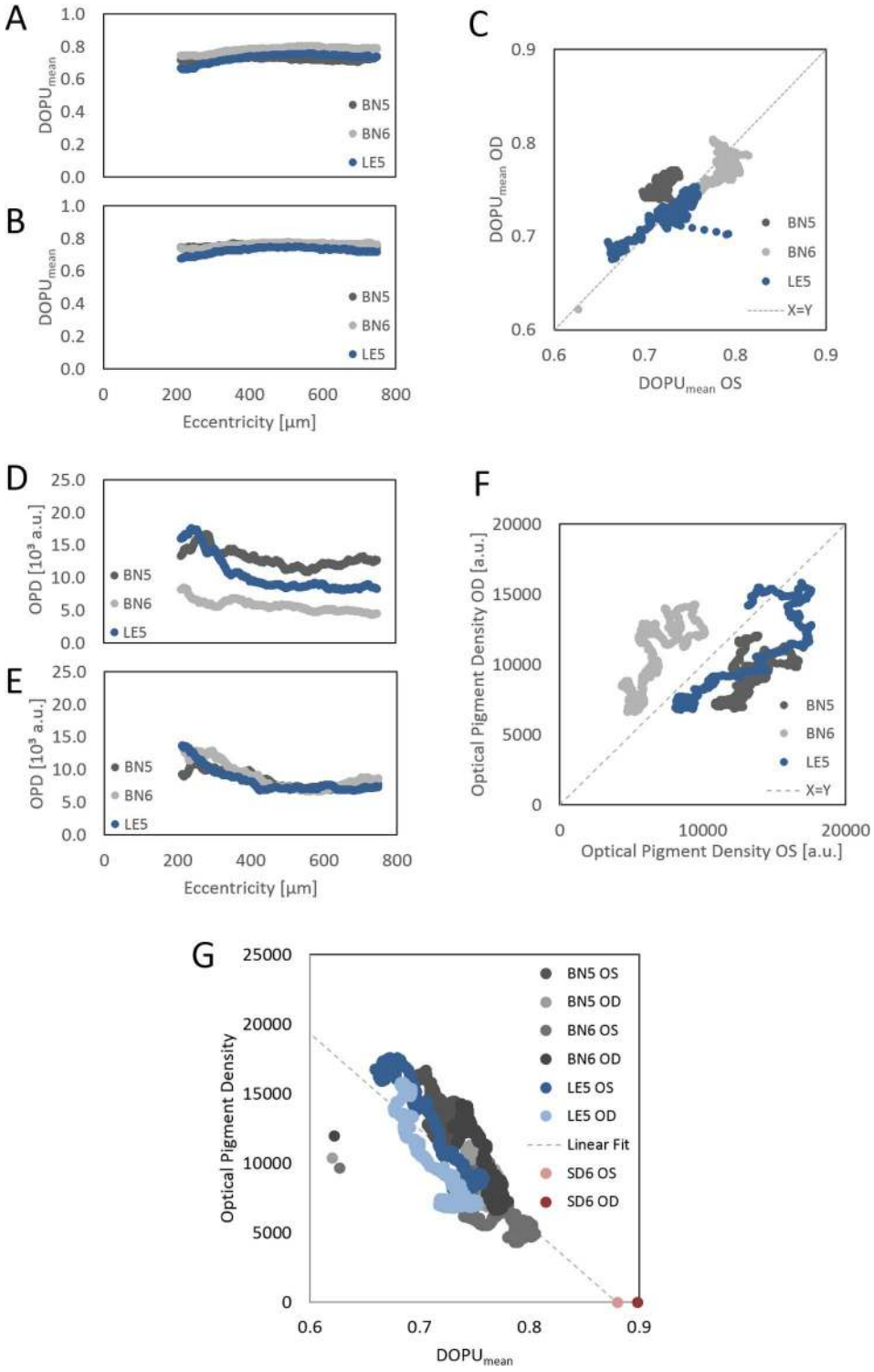

Figure 6. Analysis of melanin pigmentation in histologic serial sections versus depolarization in in vivo PS-OCT images. (**A–C**) Comparison of radial $DOPU_{mean}$ profiles in left and right eyes of pigmented rats. (**A**) Left eyes. (**B**) Right eyes. (**C**) Depolarization of left eyes versus depolarization of the corresponding right eyes at the same eccentricity. (**D–F**) Radial profiles of OPD in the same left and right eyes. (**D**) Left eyes. (**E**) Right eyes. (**F**) The OPD in left eyes versus OPD in the corresponding right eyes. (**G**) The $DOPU_{mean}$ versus OPD of both left and right eyes. A negative correlation between DOPU and OPD can be observed. The linear regression is indicated by the dashed gray line. Red circles denote the eyes of an albino rat. Different shades of gray and blue denote various pigmented animals. Animal identifiers as in Figure 4.

right eyes, respectively. These values are in the same range as the lowest $DOPU_{min}$ values measured in an earlier study in the human fovea (0.41 ± 0.07 and 0.41 ± 0.08 for the left and right eyes, respectively), where melanin pigmentation in the RPE is most dense.[20] Since the imaging configurations for human and rat retinal imaging were different, care has to be taken when directly comparing these numbers. In the eyes of albino animals, depolarization was significantly lower with

DOPU values of 0.86 ± 0.01 and 0.84 ± 0.01, respectively. Such high values are usually observed in polarization preserving or weakly birefringent tissues. In some pigmented animals (cf. Fig. 2), depolarization was also visible in the vessel walls of vasculature in the optic nerve head and in a structure we assume to be a remainder of the hyaloid canal, which connects the choroidal vasculature with the anterior eye during eye development.

The rather narrow dynamic range provided by DOPU measurements between nonpigmented (albino) and pigmented tissue is a limitation of the current DOPU detection scheme when subtle pigmentary changes should be detected. However, statistically significant differences in terms of RPE/choroid depolarization were not only found between albino and pigmented rats but also within the set of pigmented rats when comparing Brown Norway and Long-Evans rats. Interestingly, only $DOPU_{min}$ was sensitive enough to detect the difference between the strains (Brown Norway: 0.46 ± 0.06 and 0.45 ± 0.06; Long-Evans: 0.38 ± 0.03 and 0.37 ± 0.04) with $P = 0.013$ and $P = 0.011$ for the left and right eyes, respectively, whereas $DOPU_{mean}$ failed to provide a clear distinction between the two pigmented strains ($P = 0.152$ and $P = 0.099$ for the left and right eyes, respectively). In order to evaluate and potentially improve the capability of PS-OCT and DOPU to detect and delineate subtle pigmentary differences and changes, future studies in animal models of ocular hypo- and hyperpigmentation may provide further insight into the sensitivity to both local and temporal pigmentation changes.

Another limitation of the current study is the rather low axial resolution of our PS-OCT prototype, which makes it difficult to distinguish RPE from choroid in pigmented rat eyes (cf. Fig. 3). Although the native resolution of the system would enable distinction of these layers in reflectivity images, the convolution with the DOPU evaluation kernel results in a blurred image with decreased resolution. This makes it hard to study pigmentation differences between these structures based on depolarization effects. With a high-resolution PS-OCT system we recently developed for small animal retinal imaging, we aim to overcome this issue.[41] Also, the use of three-dimensional and temporal kernels for DOPU calculation can enable higher spatial resolution in the DOPU images.[42,43]

In addition to in vivo imaging of depolarization by PS-OCT, histologic serial sections were investigated. No melanin pigments were observed in histologic sections of albino rat eyes. From pigmented rat eyes, OPD fundus maps displaying the melanin pigmentation in the peripapillary region were generated. Rather uniform characteristics with a slight increase of OPD close to the ONH were observed (Fig. 6). Note, however, that unlike the DOPU profiles in Figures 6A through C, the OPD profiles differ considerably between left and right eyes (Figs. 6D–F). These differences can be attributed to fixation artifacts such as shrinking or distortions in the samples. Since such artifacts will not be observed in intact tissue, in vivo imaging is not only advantageous for the assessment of three-dimensional tissue architecture but also for the optical assessment of pigmentation compared with histologic imaging of ex vivo tissue. In the micrographs of the histologic slides, for instance, the choroid of Brown Norway rat BN5 appeared squeezed compared with the left eye. At the same time, more pigmented vessels posterior to the choroid—potentially ciliary arteries—were visible in the left eye while those were cropped in the image of the right eye. Factors like these may be responsible for an offset in the OPD profiles. Nevertheless, by analyzing the set of six eyes, intersample variations will average out to some extent, as can be observed in Figure 6G. A strong negative correlation was found between OPD and DOPU. This negative relation is not surprising. In earlier phantom experiments, we found that DOPU decreased at higher melanin concentration.[21] Unlike the experiments in artificial melanin samples there, the linear regression formula presented here enables the relation of DOPU to an actual pigmentation value in the exact same animal and tissue. Finally, this relation confirms the assumption that melanin is the cause of depolarization in the RPE.

A linear relation was found between OPD and DOPU. In our earlier investigations, we found that melanin concentration is roughly proportional to $\exp[-const \times DOPU]$.[21] The OPD depends on light extinction and therefore is a logarithmic measure. Hence, a linear relation of OPD and DOPU is reasonable. In future research using ultrastructural methods such as electron microscopy, single melanin granules in the RPE and choroid, as well as their packing density, might be assessed by quantitatively analyzing ex vivo samples. Such advanced analyses might provide the relation of DOPU values to pigment density in terms of tissue volume fraction or granules per volume.

The results presented in this article indicate that depolarization is a useful measure for the assessment of ocular melanin pigmentation. Therefore, PS-OCT may be extended from currently binary measurements of DOPU for the sake of segmentation to quantitative measurements of melanin pigmentation in the eye. This might be particularly useful for the assessment of the earliest signs of AMD, that is, pigmentary changes such as depigmentation or hyperpigmentation. Moreover, PS-OCT as a technique with high depth resolution enables the differentiation of signals originating from different layers in the posterior eye and therefore may overcome limitations of other imaging techniques such as FAF or FLIO, which only provide depth-integrated signals.

In summary, PS-OCT imaging of depolarization was demonstrated in the posterior eyes of both albino and pigmented rats. Three-dimensional images enabled the visualization of depolarizing features in vivo. The depolarization characteristics of the RPE/choroid complex were quantified and compared with postmortem histologic serial sections of the same eyes. A strong correlation between melanin pigmentation and depolarization quantified using DOPU was found. No depolarization was observed in the RPE and choroid of albino rats, which lack melanin. Our results (1) provide further evidence that melanin is the cause of depolarization in retinal PS-OCT images, (2) demonstrate that melanin pigmentation in the RPE and choroid may be quantified via depolarization imaging, and (3) suggest that PS-OCT may be a useful tool for the noninvasive quantitative assessment of pigmentary changes in vision-threatening diseases such as AMD.

Acknowledgments

The authors thank Erich Götzinger, PhD, Harald Sattmann, Siegfried Gollubits, Sandra Peiritsch, Alexandra Pernstich, and Roberto Plasenzotti, DVM, at the Medical University of Vienna for excellent technical support. Contributions of Andreas Baumann, MA, MSc, at the University of Vienna to the statistical analysis are gratefully acknowledged. Presented in part at Photonics West, San Francisco, California, United States, February 2014; at the annual meeting of the Association for Research in Vision and Ophthalmology, Orlando, Florida, United States, May 2014; and at the EURETINA Winter Meeting, Oxford, United Kingdom, January 2015.

Supported by the Medical Imaging Cluster of the Medical University of Vienna, the Austrian Science Fund (FWF Grants P19624-B02 and P25823-B24), and the European Union (FP7 HEALTH Program Grant 201880, FUN-OCT).

Disclosure: **B. Baumann**, None; **J. Schirmer**, None; **S. Rauscher**, None; **S. Fialová**, None; **M. Glösmann**, None; **M. Augustin**,

None; **M. Pircher**, None; **M. Gröger**, None; **C.K. Hitzenberger**, None

References

1. Johnson EJ. Role of lutein and zeaxanthin in visual and cognitive function throughout the lifespan. *Nutr Rev*. 2014;72:605–612.
2. Hu DN, Simon JD, Sarna T. Role of ocular melanin in ophthalmic physiology and pathology. *Photochem Photobiol*. 2008;84:639–644.
3. Kennedy CJ, Rakoczy PE, Constable IJ. Lipofuscin of the retinal pigment epithelium: A review. *Eye*. 1995;9:763–771.
4. Sparrow JR, Boulton M. RPE lipofuscin and its role in retinal-pathobiology. *Exp Eye Res*. 2005;80:595–606.
5. Styles IB, Calcagni A, Claridge E, Orihuela-Espina F, Gibson JM. Quantitative analysis of multi-spectral fundus images. *Med Image Anal*. 2006;10:578–597.
6. Jiao S, Jiang M, Hu J, et al. Photoacoustic ophthalmoscopy for in vivo retinal imaging. *Opt Express*. 2010;18:3967–3972.
7. Scoles D, Sulai YN, Dubra A. In vivo dark-field imaging of the retinal pigment epithelium cellmosaic. *Biomed Opt Express*. 2013;4:1710–1723.
8. Keilhauer CN, Delori FC. Near-infrared autofluorescence imaging of the fundus: Visualization of ocular melanin. *Invest Ophthalmol Vis Sci*. 2006;47:3556–3564.
9. Delori FC. Autofluorescence method to measure macular pigment optical densities fluorometry and autofluorescence imaging. *Arch Biochem Biophys*. 2004;430:156–162.
10. Delori FC, Dorey CK, Staurenghi G, Arend O, Goger DG, Weiter JJ. In vivo fluorescence of the ocular fundus exhibits retinal pigment epithelium lipofuscin characteristics. *Invest Ophthalmol Vis Sci*. 1995;36:718–729.
11. Pircher M, Gotzinger E, Findl O, et al. Human macula investigated in vivo with polarization-sensitive optical coherence tomography. *Invest Ophthalmol Vis Sci*. 2006;47:5487–5494.
12. Götzinger E, Pircher M, Geitzenauer W, et al. Retinal pigment epithelium segmentation by polarization sensitive optical coherence tomography. *Opt Express*. 2008;16:16410–16422.
13. Miura M, Yamanari M, Iwasaki T, et al. Imaging polarimetry in age-related macular degeneration. *Invest Ophthalmol Vis Sci*. 2008;49:2661–2667.
14. Pircher M, Hitzenberger CK, Schmidt-Erfurth U. Polarization sensitive optical coherence tomography in the human eye. *Prog Retin Eye Res*. 2011;30:431–451.
15. Schlanitz FG, Baumann B, Spalek T, et al. Performance of automated drusen detection by polarization-sensitive optical coherence tomography. *Invest Ophthalmol Vis Sci*. 2011;52:4571–4579.
16. Ahlers C, Gotzinger E, Pircher M, et al. Imaging of the retinal pigment epithelium in age-related macular degeneration using polarization-sensitive optical coherence tomography. *Invest Ophthalmol Vis Sci*. 2010;51:2149–2157.
17. Baumann B, Gotzinger E, Pircher M, et al. Segmentation and quantification of retinal lesions in age-related macular degeneration using polarization-sensitive optical coherence tomography. *J Biomed Opt*. 2010;15:061704.
18. Hong YJ, Miura M, Ju MJ, Makita S, Iwasaki T, Yasuno Y. Simultaneous investigation of vascular and retinal pigment epithelial pathologies of exudative macular diseases by multifunctional optical coherence tomography. *Invest Ophthalmol Vis Sci*. 2014;55:5016–5031.
19. Schuetze C, Wedl M, Baumann B, Pircher M, Hitzenberger CK, Schmidt-Erfurth U. Progression of retinal pigment epithelial atrophy in antiangiogenic therapy of neovascular age-related macular degeneration. *Am J Ophthalmol*. 2015;159:1100–1114.
20. Baumann B, Gotzinger E, Pircher M, Hitzenberger CK. Measurements of depolarization distribution in the healthy human macula by polarization sensitive OCT. *J Biophoton*. 2009;2:426–434.
21. Baumann B, Baumann SO, Konegger T, et al. Polarization sensitive optical coherence tomography of melanin provides intrinsic contrast based on depolarization. *Biomed Opt Express*. 2012;3:1670–1683.
22. Schuetze C, Ritter M, Blum R, et al. Retinal pigment epithelium findings in patients with albinism using wide-field polarization-sensitive optical coherence tomography. *Retina- J Ret Vit Dis*. 2014;34:2208–2217.
23. Götzinger E, Pircher M, Baumann B, et al. Speckle noise reduction in high speed polarization sensitive spectral domain optical coherence tomography. *Opt Express*. 2011;19:14568–14585.
24. Hughes A. A schematic eye for the rat. *Vis Res*. 1979;19:569–588.
25. Baumann B, Rauscher S, Glosmann MG, et al. Peripapillary rat sclera investigated in vivo with polarization-sensitive optical coherence tomography. *Invest Ophthalmol Vis Sci*. 2014;55:7686–7696.
26. Feeney-Burns L, Hilderbrand ES, Eldridge S. Aging Human RPE - Morphometric analysis of macular, equatorial, and peripheral cells. *Invest Ophthalmol Vis Sci*. 1984;25:195–200.
27. Kornzweig AL. Aging of the retinal pigment epithelium. In: Zinn KM, Marmor MF, eds. *The Retinal Pigment Epithelium*. Cambridge, MA: Harvard University Press; 1979:478–495.
28. Srinivasan VJ, Monson BK, Wojtkowski M, et al. Characterization of outer retinal morphology with high-speed, ultrahigh-resolution optical coherence tomography. *Invest Ophthalmol Vis Sci*. 2008;49:1571–1579.
29. Schmitz-Valckenberg S, Holz FG, Bird AC, Spaide RF. Fundus autofluorescence imaging - Review and perspectives. *Retina-J Ret Vit Dis*. 2008;28:385–409.
30. Spaide RF. Enhanced depth imaging optical coherence tomography of retinal pigment epithelial detachment in age-related macular degeneration. *Am J Ophthalmol*. 2009;147:644–652.
31. Klein R, Chou C, Klein BK, Zhang X, Meuer SM, Saaddine JB. Prevalence of age-related macular degeneration in the US population. *Arch Ophthalmol*. 2011;129:75–80.
32. Sekiryu T, Iida T, Maruko I, Saito K, Kondo T. Infrared Fundus Autofluorescence and central serous chorioretinopathy. *Invest Ophthalmol Vis Sci*. 2010;51:4956–4962.
33. Duncker T, Marsiglia M, Lee W, et al. Correlations among near-infrared and short-wavelength autofluorescence and spectral-domain optical coherence tomography in recessive Stargardt disease. *Invest Ophthalmol Vis Sci*. 2014;55:8134–8143.
34. Kellner U, Kellner S, Weinitz S. Fundus autofluorescence (488 nm) and near-infrared autofluorescence (787 nm) visualize different retinal pigment epithelial alterations in patients with age-related macular degeneration. *Retina-J Ret Vit Dis*. 2010;30:6–15.
35. Schmitz-Valckenberg S, Fleckenstein M, Helb HM, Issa PC, Scholl HPN, Holz FG. In vivo imaging of foveal sparing in geographic atrophy secondary to age-related macular degeneration. *Invest Ophthalmol Vis Sci*. 2009;50:3915–3921.
36. Greenberg JP, Duncker T, Woods RL, Smith RT, Sparrow JR, Delori FC. Quantitative fundus autofluorescence in healthy eyes. *Invest Ophthalmol Vis Sci*. 2013;54:5684–5693.
37. Cideciyan AV, Swider M, Jacobson SG. Autofluorescence imaging with near-infrared excitation: normalization by reflectance to reduce signal from choroidal fluorophores. *Invest Ophthalmol Vis Sci*. 2015;56:3393–3406.

Investigative Ophthalmology & Visual Science

38. Dysli C, Dysli M, Enzmann V, Wolf S, Zinkernagel MS. Fluorescence lifetime imaging of the ocular fundus in mice. *Invest Ophthalmol Vis Sci*. 2014;55:7206–7215.
39. Jiao S, Yao G, Wang LV. Depth-resolved two-dimensional Stokes vectors of backscattered light and Mueller matrices of biological tissue measured with optical coherence tomography. *Appl Opt*. 2000;39:6318–6324.
40. Ansorge M, Sahlmann B, Stanka P. On the melanization of the rat's eye. *Pigm Cell Res*. 1996;9:142–147.
41. Fialová S, Rauscher S, Gröger M, Pircher M, Hitzenberger CK, Baumann B. High-resolution polarization sensitive OCT for ocular imaging in rodents. In: *Optical Coherence Tomography and Coherence Domain Optical Methods in Biomedicine XIX*. Fujimoto JG, Izatt JA, Tuchin VV. San Francisco, CA: SPIE; 2015. Paper 93120T.
42. Bonesi M, Sattmann H, Torzicky T, et al. High-speed polarization sensitive optical coherence tomography scan engine based on Fourier domain mode locked laser. *Biomed Opt Express*. 2012;3:2987–3000.
43. Sugita M, Pircher M, Zotter S, et al. Analysis of optimum conditions of depolarization imaging by polarization-sensitive optical coherence tomography in the human retina. *J Biomed Opt*. 2015;20:016011.

Investigative Ophthalmology & Visual Science